REVISTA DE METALURGIA, 49 (3)
MAYO-JUNIO, 178-199, 2013
ISSN: 0034-8570
eISSN: 1988-4222
doi: 10.3989/revmetalm.1223

A review of ordering phenomena in iron-silicon alloys(•)

F. González* and ** and Y. Houbaert*

Abstract

Silicon steel is an industrially-desired alloy of iron and silicon, characterised by soft magnetic properties, low eddy-current losses, and low magnetostriction. Silicon steels have narrow hysteresis cycles, making them particularly advantageous in applications using electromagnetic fields, such as transformers, generators, electric motor cores, and few other components in industry. Despite its incontestable industrial value, there is not much agreement on the atomic structure of silicon steel. Gaining better understanding of e.g. ordering processes in Fe-Si alloys could not only explain their magnetic properties, but also open opportunities to reduce their weaker characteristics, such as brittleness that adversely affects silicon steel workability and its associated high production costs. This review summarises the state-of-the-art knowledge about ordering in silicon steel and describes the most relevant experimental techniques used for studying its microstructure. In addition, the process of building the iron rich part of the Fe-Si phase diagram is explained. Lastly, the influence of order on the alloy's magnetic and mechanical properties is illustrated.

Keywords

Ordering; Iron-silicon alloys; Intermetallic phases; Mechanical properties; Phase diagram.

Revisión de fenómenos de orden en aleaciones hierro-silicio

Resumen

El acero al silicio es una aleación de importancia industrial, caracterizada por propiedades magnéticas blandas, bajas pérdidas por corrientes de Foucault y baja magnetostricción. Los aceros al silicio tienen ciclo de histéresis estrecho, lo que es una ventaja en aplicaciones con campos electromagnéticos, como transformadores, generadores, núcleos de motores eléctricos y otros componentes industriales. A pesar de su incomparable valor industrial, no hay convenio sobre la estructura atómica del acero al silicio. Obtener mayor conocimiento sobre los procesos de orden no sólo podría explicar las propiedades magnéticas sino que también podría abrir vías para la reducción de sus características más débiles, como su fragilidad, la cual afecta negativamente a la fabricación del acero al silicio y se asocia con altos costes de producción. Esta revisión resume los últimos conocimientos sobre orden en acero al silicio y describe las técnicas experimentales más importantes usadas para estudiar su estructura. Además, se da una explicación sobre la construcción de la parte rica en hierro del diagrama de fases del Fe-Si. Por último se ilustra la influencia del orden en las propiedades magnéticas y mecánicas.

Palabras clave

Orden; Aleaciones hierro-silicio; Fases intermetálicas; Propiedades mecánicas; Diagrama de fases.

1. INTRODUCTION

1.1. Historical review

The first artificial introduction of silicon into iron dates from the beginning of the 19th century when the two elements were first melted together[1]. In the field of soft magnetic materials the 19th century was a period of major breakthroughs including the first studies of Fe-Ni alloys and research on magnetization and hysteresis for different steels and geometries. During this period, the basis of the systematic research of electromagnetic properties of solids was laid, as published by Ewing in 1890 and 1900 [2].

Nonetheless, initially silicon steel did not receive much attention. In 1880 it was already well known that addition of silicon into iron produces harder steel, but also that, after certain quantity of silicon is exceeded, the alloy's brittleness increases fast. The studies of magnetic properties of silicon steel were controversial and not definite until the beginning of the 20th century. Since 1900 silicon has become commercially alloyed with iron after Sir R. Hadfield ultimately proved that Fe-Si steel displays improved soft magnetic properties as compared to the purest

(•) Trabajo recibido el día 3 de mayo de 2012 y aceptado en su forma final el día 4 de febrero de 2013.
* Department of Materials Science and Engineering, Ghent University, Technologiepark 903, BE-9052, Gent Zwijnaarde, Belgium.
** Parque Científico Universidad de Valladolid, Edificio I+D, Pº Belén, 11 - Campus Miguel Delibes, ES-47011, Valladolid, Spain.

iron that could be forged at those times[3]. Soon thereafter, techniques such as electrolytic deposition and melting *in vacuo* allowed for improving the magnetic properties of pure iron[4]. Initially, the first theories proposed that silicon mainly influences alloy properties through reduction of iron oxides, causing decarburization and a slight increase of resistivity. However, later developments using combination of melting iron *in vacuo* and alloying it with silicon dramatically improved the permeability and magnetic properties of silicon steel[5 and 6]. As early as in 1915, it was concluded that another mechanism had to be responsible for this improvement[1], aside from deoxidation and decarburation. The first explanations came few years later with the theory of order.

The development of the superlattice theory has been reviewed by other authors like Birchenall, Muto *et al.*, Cullity and Guruswamy[7-10]. According to Birchenall and Muto *et al.*[7 and 8], Tamman reported the first superlattices in 1919, following chemical considerations, for Au-Cu alloys. Four years later, using same alloys, Bain observed the superlattice lines with X-ray diffraction (as explained by Cullity[9]). Next, in 1932, Bradley described ordering in ferroalloys for the alpha-phase of Fe-Al alloys according to Guruswamy[10], and in 1933, Greiner, Marsh and Stoughton published a book *The Alloys of Iron and Silicon*[11] already referencing the ordering and superlattices in the Fe-Si system, although the first theories of ordered Fe-Si date only from mid-twenties[12].

Later, most of the research on soft magnetic materials was conducted by the industry. Here, the methods of improving manufacture and production quality were defined allowing the best soft magnetic properties. The improvement of texture led to the development of grain oriented steel (Goss texture), in which most of the grains' structures share a determined orientation with respect the laminated sheet[13]. This steel is mostly used in applications where the direction of easy magnetisation is fixed. In addition, grain growth and precipitation[14 and 15] were better controlled. Alternative production routes and optimisation of industrial thermomechanical routes[16-18] were proposed. For instance, hot dipping and diffusion annealing processes have been studied[19]. High-energy ball milling techniques were applied for mechanical alloying[20]. Other processes include the Chemical Vapour Deposition (CVP), which enables the production of high silicon steel by the chemical reaction of gases as $SiCl_4$ [21] or SiH_4 [22] on a cold rolled, medium Si-content sheet of thickness between 0.1 and 0.05 mm [23]. The silicon forms bond with the iron, and high-silicon steel is obtained in the form of thin sheets. It is a commercially viable solution although it is expensive and ecologically detrimental due to the waste material (for instance, $FeCl_2$ [24]).

The last big breakthrough in soft magnetic materials research took place in the decade of 1970 with the development of nanocrystalline ribbons, a material displaying different degrees of crystallinity including amorphous state. Its main advantage is the possibility to obtain the optimal content of silicon, Fe-6.5 mass % Si, for the best soft magnetic properties (for instance, almost zero magnetostriction), with avoiding the problem of brittleness. The process consists in a rapid quench of molten material on a spinning wheel, resulting in formation of a ribbon[25] which can be manipulated for obtaining a desired microstructure and texture[26].

In equilibrium conditions there is a compositional gap between the start of embrittlement and the appearance of order. While the steel is difficult to work at compositions as low as 6 at. % Si (3.5 mass % Si), experimental data show superlattices (hence order) near 11 at. % Si (5 mass % Si). The structure between 6 at. % Si and 11 at. % Si is ferrite (α), according to the Fe-Si phase diagram (analysed in section 1.3). If the ordering is responsible for lack of workability, at these low Si-contents the structure should be disordered, hence workable. Despite this, the steel is not workable anymore and cracks appear during rolling. While metastable conditions and short-range order have been proposed to explain this phenomenon[27], more studies are required to define properly the cause of embrittlement.

1.2. Statistical treatment of order

The Bragg-Williams-Gorski (BWG) statistical theory for long-range ordered systems describes the energy behaviour, transition temperatures and equilibrium states from the definition of a long-range parameter *s*. This Bragg-Williams parameter[28] is related to the entropy *S* of a system, and it describes the configurational space. The value of *s* varies between 0 (disorder) and 1 (total order). The free energy *F* is calculated as function of temperature and composition, so the limits of ordered phases (transition temperatures, etc.) can be analysed. The theory of ordering was developed for Fe-Si alloys using BWG theory on the basis of experimental observations that revealed similar diffraction spots to those of CsCl and Fe_3Al structures. Therefore, the following assumptions are made for the formulation of *s*:

a) The superlattice consists of four interpenetrated fcc cells, with a lattice parameter double than that of a single (bcc) lattice. The atoms in two sublattices

are nearest-neighbours (nn) with the atoms of the other two, in a configuration of 8 bcc piled up as a cube.

b) Homogeneous distribution and long-range order is considered. Then, *s* will depend on the probability that each lattice site is occupied by an iron or a silicon atom, for each sublattice[29].

The calculation of the free energy accounts for the interaction energies to nn and next-nearest neighbour (nnn), namely W and w. Three configurations are possible: for equal probability of occupation in any sublattice (disorder, with α ferritic structure), for probability that the nn are inequivalent (tendency to B2, with the so-called α_2 structure) and, finally, for probability that the nn and nnn are inequivalent (tendency to $D0_3$, namely α_1). The value of entropy depends of the number of configurations.

The free energy ($\Delta F = \Delta U - \Delta TS$) is calculated, following Inden[30]:

For α_2

$$F(s) = U_0 - Nc_Ac_B(4W + 3w) - N/2[(8W - 6w)(½ (P_A^I - P_A^{III})^2) + (¼) Nk_BT [2P_A^I \log P_A^I + 2P_A^{III} \log p_A^{III} + 2P_B^I \log P_B^I + 2P_B^{III} \log P_B^{III}]$$

For α_1

$$F(s) = U_0 - Nc_Ac_B(4W + 3w) - N/2 [(8W - 6w)(¼ (2P_A^I - P_A^{III} - P_A^{IV})^2] + (¼) Nk_BT [2P_A^I \log P_A^I + P_A^{III} \log P_A^{III} + P_A^{IV} \log P_A^{IV} + 2P_B^I \log P_B^I + 2P_B^{III} \log P_B^{III} + P_B^{IV} \log P_B^{IV}]$$

The composition is given by c_A and c_B in a system with N atoms, and the probability of occupation of atom A in the sublattice j is P_A^j. In addition, three parameters related to the short order parameter can be defined from the occupation probabilities[29] as follows:

$$s_x = ¼ (P_A^I + P_A^{II} - P_A^{III} - P_A^{IV})$$

$$s_y = ½ (P_A^{III} - P_A^{IV})$$

$$s_z = ½ (P_A^I - P_A^{II})$$

The configurations α_2 ($s_x \neq 0$, $s_y = s_z = 0$) and α_1 ($s_x \neq 0$, $s_y \neq 0$, $s_z \neq 0$) are depicted in figure 1 (left and right are α_2 and α_1, respectively, drawn with VESTA software[31]). They are a variation of the disordered bcc α ($s_x = s_y = s_z = 0$). In an ordered compound formed by 2 different atoms A and B, the lattice sites can be separated into A and B sites, and the relative position of these sites determines the type of order. In case of ordering, iron atoms will tend to occupy A sites, and silicon atoms will tend to occupy B sites.

The equilibrium condition is obtained from: $\partial F/\partial s_m = 0$; $\partial^2 F/\partial s_m \partial s_n > 0$; where m, n = x, y, z. Each configuration is associated with a given set of occupation probabilities and with a transition temperature, obtained from the equilibrium condition.

With these configurations, it is possible to define two critical temperatures of transition[29 and 32] from α to α_2 and from α_2 to α_1. The first transition temperature have the form of:

$$T_x k_B = (8W - 6w) c_{Si} (1 - c_{Si})$$

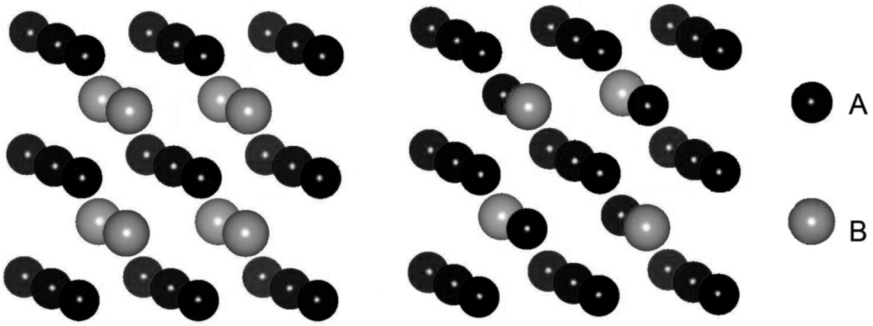

Figure 1. Different: B2 (left) and $D0_3$ (right) configurations. A: sites correspond to high probability of occupation by iron, B: sites correspond to higher probability of occupation by silicon atoms. Figures produced with VESTA software[31].

Figura 1. Configuraciones distintas: B2 (izquierda) y $D0_3$ (derecha). Los puntos A corresponden a puntos con alta probabilidad de ocupación por hierro, los B corresponden a alta probabilidad de ocupación por átomos de silicio. Las imágenes se han realizado con el programa VESTA[31].

Under this first transition temperature, 2 nnn sublattices (in Fig. 1, B sites) are equiprobable.

In a bcc-type lattice, the W and w are the interaction energies between 8 nn and between 6 nnn, respectively. They are supposed to be independent of the temperature and concentrations c_{Si} and $c_{Fe} = (1 - c_{Si})$. Of note, this independence is not followed in case in Fe-Al alloys, for instance[32].

For the second transition temperature, three of the sublattices become equiprobable and it is said that there are ordering reactions in nnn. If this probability is x, then the configuration of the minimum x at the second transition temperature $x_{min}(T_y)$ will affect the ordering temperature:

$$T_y k_B = 6w (c_{Si} - x_{min}) (1- c_{Si} + x_{min})$$

The values of the interaction energies W and w are calculated by adjusting them to the experimental observations. Then, the α-α_2 and α_2-α_1 phase transformation lines can be drawn in the phase diagram, as shown in the next section. The tentative values calculated according to this method are shown in table I.

In addition, the α_2 transformation line was recalculated under the Curie temperature by Swann *et al.*[32] in order to include ferromagnetic interactions[5]. It is analogous to the first transition temperature but with taking into account ferromagnetic atoms and using the magnetic interaction energies M and m, instead of W and w: $T_c k_B = (8M - 6m)(1 - c_{si})$, M and m are obtained empirically as a function of c_{Si}. Nonetheless, this correction is small and it is not depicted in the Kubaschewski diagram. The main difference between both phase diagrams is the existence of the B2+$D0_3$ either strictly under the Curie temperature (Swann[32]) or extended up to 700 °C (Kubaschewski[33]).

If the content of silicon reaches 25 at. %, the B sites will correspond to silicon atoms in the figure 1 (right) in the completely ordered configuration. For Si-content of 50 %, instead of the proper B2 structure (Fig. 1 left), the configuration B20 is stable, but it is not based on a bcc lattice and it is accompanied by a change of symmetry.

Bethe's theory is a study of order, considering configurations of neighbouring atoms. The configuration study can be done using the nearest neighbour, next-nearest neighbour, etc. A short-range order parameter s is defined, explaining the excess energy at transition temperatures (where there is no long-range order, but short-range order still exists[8]). The estimation of both *s* using Mössbauer spectroscopy data gives important information about the atom distribution as function of Si-content. This shall be described in section 2.2.

As expected, Bethe's theory leads to equivalent results as the BWG approximation for long-range order[8].

In summary, experimental evidence suggest the existence of $D0_3$ ordered superstructure for Si-contents under 25 at. %. Basing on this lattice, different atomic configurations are predicted as a function of the temperature, Fe/Si ratio, and energy of interaction between atoms. Further experimental studies served to fit the variables of the theory, so it reproduces (most of) the experimental behaviour observed. Hence, the phase diagram is formed. This is further explained in the next section.

Table I. Calculated interaction energies between first and second neighbours

Tabla I. Energías de interacción calculadas entre los primeros y segundos vecinos

	Inden, Pitsch[29]	Swann, Granas[32]
W	0.1733 eV	0.1699 eV
w	0.0862 eV	0.0862 eV

1.3. Phase diagram and its origins

The phase diagram for the Fe-Si system has changed much over the years, its shape being defined by theoretical considerations of configurational energies[29] and experimental data. The phase diagram published by Kubaschewski[33] (Fig. 2) is the most commonly accepted one, and it attempts to include the majority of theoretical and experimental studies performed in the Fe-Si system.

As shown in the diagram, the solid solubility of silicon in iron extends to the value of 25 at. % at RT and to about 30 at. % (12.1 to 14.2 mass. %) between 1050 and 1200 °C. Silicon stabilizes the bcc α-phase. Of note, the γ-phase region of the diagram disappears when the Si-content increases above 3.8 at. % (2 mass. %). There is a so-called 'gamma loop' between the α- and γ-regions, which will not be covered further in this work as it concerns only bcc silicon steel, stable between Si-contents of 3.8 and 25 at. % (2 and 12.1 mass %) up to melting temperatures[34].

The atomic radius of iron is 0.126 nm while the atomic radius of silicon is 0.132 nm, therefore their solid solution will have a substitutional character.

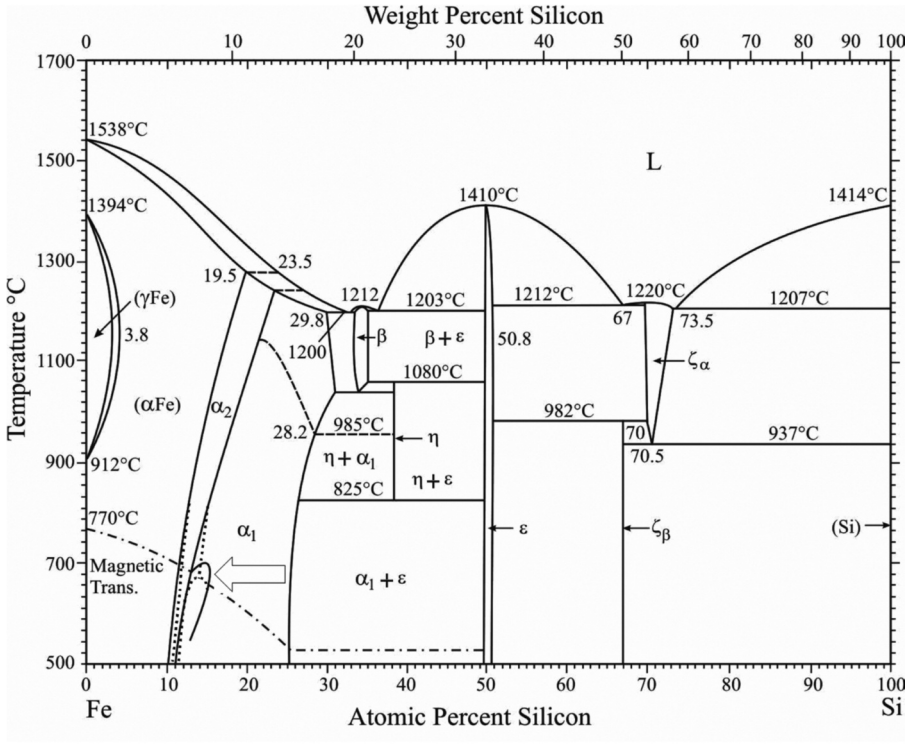

Figure 2. Kubaschewski phase diagram for the Fe-Si system[33]. The white arrow marks a double-phase field (B2+$D0_3$). The thin black arrows designate phases. Dotted lines between 10 and 15 at. % indicate the phase transition according to Swann *et al.*[32].

Figura 2. Diagrama de fases del sistema Fe-Si según Kubaschewski[33]. La flecha blanca gruesa señala la región de doble fase. Las flechas finas negras señalan fases. Líneas punteadas entre 10 y 15 at .% indican la transición de fase de acuerdo con Swann et al.[32].

Silicon atoms exchange positions within the bcc iron-structure; therefore, a disordered solid solution can be expected.

First, a homogeneous distribution will be considered in a bcc lattice. This means that silicon atoms will most probably be surrounded by iron atoms. When silicon concentration reaches 6.25 at. % (3.3 mass %, which is coincidentally the practical limit for industrial lamination), there is one silicon atom every 16 atoms. This corresponds to eight bcc cells which fill the space. Ideally, each silicon atom will be surrounded by iron atoms up to the fourth neighbour in a homogeneous $Fe_{15}Si$. This configuration has been described with Mössbauer experiments serving as basis[35 and 36].

When silicon concentration increases to 12.5 at. % (6.45 mass %), there will be two silicon atoms every eight cells on average. Thus, in a completely homogeneous solution, the phase will on average be Fe_7Si.

Upon increasing Si-content, at 25 at. % (12.1 mass %) there are four silicon atoms in eight cells, each silicon atom surrounded by iron atoms up to the second nearest neighbour. This is the $D0_3$ structure, according to the Strukturbericht-designation. Increasing Si-content to about 50 at. % (21.6 mass %) would lead to the structure of stoichiometric FeSi.

When interaction energies are included, this homogeneous model is not suitable. The BWG model is more appropriate to describe the phase transitions. As a natural result of the BWG applied to the $D0_3$ structure, additional lines appear in the homogeneous solid solution part of the diagram, while the elemental structure is still bcc, as analysed in the previous section. At low Si-content, there is a domain of random solid solution of iron and silicon with a bcc structure, called a in the diagram and also A2 in other literature (Strukturbericht-designation). The changes of configurations may be not be first order.

Curie temperature depends on the Si-content, as seen before[5 and 6]. Considering the region of the phase diagram over Curie temperatures (the paramagnetic region), an ordered superstructure called α_2 is possible

for a Si-content over 13 at. % (6.4 mass %). This superstructure was proposed due to the decrease of the X-ray diffraction (111) line, typical for $D0_3$, while the (200) line, typical of B2 order, became stronger after the sample was quenched[37]. TEM and neutron diffraction experiments reported presence of B2 and absence of $D0_3$ for different thermal treatments on a range of Si-contents[38-41]. Currently this phase is known in literature as the B2 phase, according to the Strukturbericht-designation. It is characterised by a crystal structure similar to the CsCl unit cell. Nevertheless, for iron silicon the concentration of silicon in this region is far below the 50 at. %, which would be necessary for a fully ordered microstructure corresponding to the stoichiometric formula FeSi. In fact, the intermetallic compound FeSi appears in the phase diagram. The structure of FeSi structure is not bcc but B20 [42-44] as explained in the previous section. Some authors reject the existence of B2 ordering at low Si-contents[45], considering it as an incomplete $D0_3$ ordering. The group of Nembach presents evidence of $D0_3$ ordering in a region typically considered α_2, in neutron diffraction experiments as it will be seen in section 2.3.2 (Neutron diffraction). In this case, the BWG can still be applied, recalculating the values for atomic interaction to nearest and next-nearest neighbours (W and w). This work will use the preferred term α_2, meaning that the structure is bcc, with certain occupation of silicon in the center of the lattice. Two main arguments support the use of this notation: the controversy with respect the existence of the B2 region, and the fact that B2 is, strictly speaking, the name of a binary phase that does not take actually place when the Fe-Si system becomes binary (as mentioned before).

For Si-contents between 13 to 25 at. % (6.4 to 11.6 mass %), upon increasing the Si-content, the phase overcomes the transition $\alpha - \alpha_2 - \alpha_1$ at the temperatures calculated with the BWG model and adjusted to experimental results from, for example, DSC or neutron diffraction techniques[46-48]. The α_1 order is considered as an incomplete $D0_3$ superstructure, formed by 8 bcc cells with 12 iron atoms and 4 silicon atoms arranged in 4 fcc sublattices, as discussed in the previous section (the BWG model). The proper $D0_3$ configuration contains 4 silicon atoms at the centre of the stacked lattices, with maximum distance between them, and 12 iron atoms. On the other hand, the α_1 configuration is just the tendency of atoms to occupy the positions following the $D0_3$ configuration: silicon atoms will tend to occupy the centre of the bcc in the same manner as in the $D0_3$, iron atoms will occupy the other three sublattices, and the rest of unoccupied sites in the silicon sublattice will be filled by iron.

At higher temperatures, the phases change slowly, following a second order transition. The higher the temperature, the more Si-content is needed for the transition. Therefore, it is possible that alloys containing certain concentrations of silicon present a certain degree of order at low temperatures but show disorder at higher ones.

The reasoning is similar under Curie temperatures (within the ferromagnetic region[5]). The ordered superstructure called α_2 is possible for a Si-content over 10 at. % (5.2 mass %) at 500 °C. However, due to magnetic interaction, there is a double-phase zone marked with a white arrow in figure 2. The structure is formed by a mixture of two ordered phases, called α_2 and α_1 order. This double-phase zone is separated from higher temperatures by a first-order transition[49] and it was described using diffraction and imaging techniques[32]. The limit of the double-phase zone is disputed between Swann *et al.*[32] and Kubaschewski[33]. Swann studied the interactions considering the influence of ferromagnetism, and the double-phase region is limited strictly under the Curie temperature. On the other hand, Kubaschewski considers that the double-phase region is extended slightly over the Curie temperature.

Upon further increasing Si-content, the structure becomes $D0_3$, which has been described as forming ordered domains that increase in size with Si-content. After Si-content surpasses 25 at. % (12.11 mass %), the structure starts showing B20 ordering, but is not a bcc structure anymore as stated before.

While the atomic structure is influenced by the ferromagnetism, the amount of silicon in turn reduces the Curie temperature, due to the decrease of iron atoms in the lattice[5,6 and 47]. When Si-content reaches 25 at. %, the Curie temperature is stable until the structure becomes paramagnetic, upon reaching 50 at. %.

2. DETECTION OF ORDERING

Ordered structures present a lesser degree of symmetry than disordered structures and can be described using two or more sublattices. Each sublattice is associated with one kind of atom. In a disordered lattice, some families of planes will produce destructive interference and the diffracted beam will give zero intensity for certain directions. For instance, a diffraction experiment in a bcc structure will contain no reflections from planes whose indices follow the so-called extinction rule h+k+l = n, where n is an odd number.

Nonetheless, ordered structures have different elements forming planes which belong to the same

family. The destructive interference will give non-zero intensity for these directions. Then, forbidden reflections will appear in bcc ordered structures. These reflections receive the name of 'superlattice reflections' because they are common from superlattice structures. It is possible to determine the type of superstructure by analysing these forbidden reflections. This is further explained in section 2.3 (Diffraction techniques).

Another way to detect ordering is the analysis of the ordering transformation itself. A change of symmetry corresponds to interchange of energies[50], and a number of techniques are based on this principle. Differential scanning calorimetry is one of the most important ones.

Other techniques include measuring properties that allegedly change with order, such as resonance of high-energy radiation or electrical resistance[51 and 41].

2.1. Differential Scanning Calorimetry (DSC)

Differential scanning calorimetry is based in the continuous isothermal heating of a sample and a reference. The temperature changes at the same rate in both, and the difference between heating rate of a sample and the reference is measured. There is an endotermic reaction if the heating rate of the sample increases with respect to the reference's, and conversely, if the heating rate decreases the reaction is exotermic. A reaction with a change of latent heat is a first-order transition (for instance melting) while ferromagnetic or symmetry transitions are second-order transitions.

DSC gives information of the temperatures at which phase transformations take place. It also is sensitive to recrystallisation and recovery, so in order to show only phase transitions the sample normally is annealed first (in our case, only the second run is shown although it does not greatly changes from the first one).

As commented, the Curie transition temperature (from ferromagnetic to paramagnetic phase with increase of temperatures) decreases with increasing Si-content[5 and 47] for compositions under the stoichiometric Fe_3Si content, as described by Swann[32]. As it can be seen in figure 3, the Curie transition for compositions over 14 at. % the T_c is close to 680 °C, in agreement with the phase diagram (for pure iron the T_c is 770 °C). DSC was used by Yuan[52] to determine the relationship between Curie temperature and solid solubility of silicon in iron.

Figure 3 gives additional information. Aside of the Curie temperature near 680 °C, a relatively small transition takes place near 570 °C. It seems to be a second-order transition, a change of heat capacity more noticeable when plotting the specific heat. For this Si-content, the only transition expected in the ferromagnetic region would be an order transition, from the configuration α_1 to the region known in literature as double-phase region (marked with an arrow in Fig. 2), $\alpha_1 \rightarrow \alpha_2 + \alpha_1$. Silicon in $D0_3$ sites

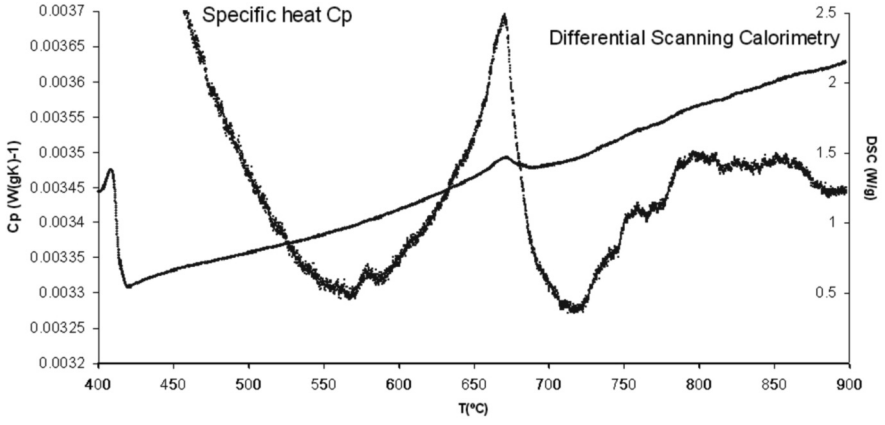

Figure 3. Second heating cycle of a Fe-13.88 at. % after hot rolling. The first cycle contains recrystallisation features that do not appear in the present run. Peak corresponding to Curie transition appears near 680 °C.

Figura 3. Segundo ciclo de calentamiento de Fe-13,88 at. % después de laminado en caliente. El primer ciclo contiene características de recristalización que no aparecen en el ciclo presentado. El pico correspondiente a la transición de Curie tiene lugar cerca de 680 °C.

start jumping out of their equilibrium positions. Then, some zones display more concentration of silicon without forming clustering.

For temperatures higher than T_c, the transition from the double phase is close to the limit between α_2 and α_1. A complicated set of transformations may be taking place, but it is hard to separate them from the background noise.

2.2. Mössbauer spectroscopy

Mössbauer spectroscopy provides information about interaction between neighbouring atoms, using γ radiation. When γ rays interact with liquids or gasses, atomic resonance is not detected due to Doppler effect and recoil. On the other hand, the atoms are bonded to a lattice in a solid, so there is a probability that the interaction does not involve phonons. This produces a recoil of the whole specimen. Thus, the recoil energy of individual atoms is negligible, and there is a detectable resonance of the γ rays. The usual γ ray source is ^{57}Fe.

The resonance frequency and Doppler effect give information of the hyperfine interaction of an atom with its surrounding neighbours. Hence the information obtained is related to the local configuration of the atoms next to the iron atoms.

In figure 4, different Mössbauer spectra[53], corresponding to four samples with different Si-content, show the main six peaks displayed by ultra-low carbon steel, plus extra peaks that change the profile of the whole spectrum. The shape of this profile changes for each different Si-content. These peaks arise from the interactions between iron and silicon atoms. It has been observed that the fitting of the Mössbauer spectra is more exact with the configuration of silicon atoms being surrounded up to the third and fourth neighbour by iron atoms. Consequently, presence of Fe_7Si and, especially, $Fe_{15}Si$ stoichiometries in Fe-Si alloys was reported to particularly improve the Mössbauer spectra fitting[35 and 36]. As it is a local technique, the spectrum changes when the surrounding local atomic configuration changes, for instance when the Si-content changes or deformation is applied. Section 3.1 (Embrittlement and order) presents some results of Mössbauer spectra for different Si-contents and deformations.

2.3. Diffraction techniques

When a crystalline material is irradiated by an electromagnetic beam, if the lattice separation is comparable with the wavelength of the probe radiation, the latter diffracts accordingly to the spacing, packing and orientation of the lattice.

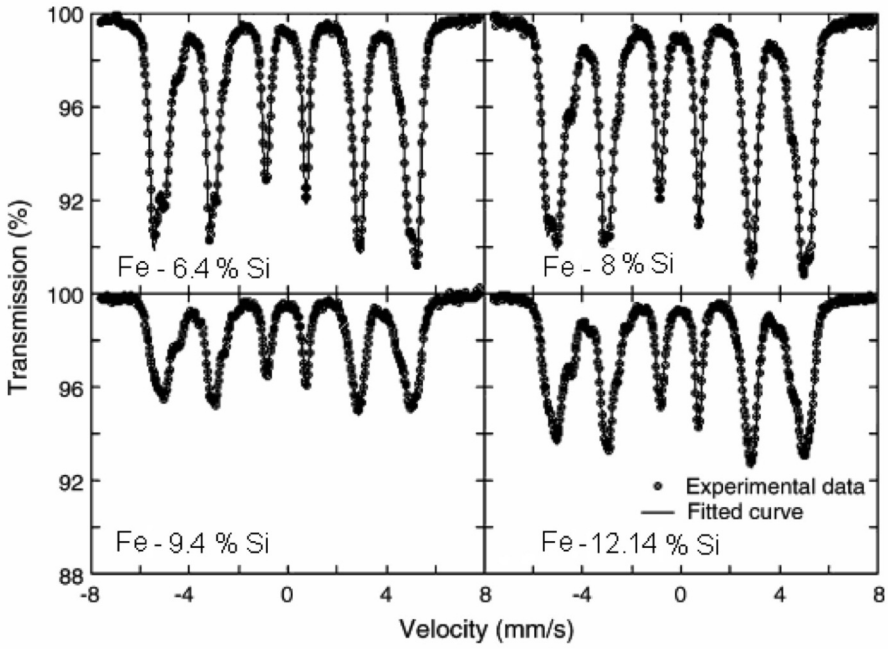

Figure 4. Mössbauer measurements for different contents of silicon (in at. %) (from[53]).

Figura 4. Medidas Mossbauer para distintos contenidos de silicio (en at. %) (de[53]).

The diffracted wave is proportional to the structure factor, which depends of the diffracting plane orientation and of the atomic basis[54]:

$$F(\Delta k) = \sum_{r_k}^{basis} f_{at}(r_k) \cdot \exp(-i2\pi\Delta k \cdot r_k)$$

The vectors r_k and Δk correspond to the interacting atomic plane direction and the scattered radiation, respectively, and $f_{at}(r_k)$ is the scattering factor of the atom. There are cases when the sum is null, due to the exponential factor: for certain plane families, the wave will be out of phase after diffracting with one family of planes. Because the planes sharing the same direction have all the same scattering factor, destructive interference takes place. This produces directions with no intensity, also called forbidden reflections[9]. Based on these sets of reflections, it is possible to define an extinction rule. Different types of lattices (bcc, fcc, hcp...) have different extinction rules. As seen in the introduction of this section, the extinction rule for bcc lattice is h + k + l = n, with n odd.

Diffraction obeys the normal extinction rules in a disordered crystalline specimen. Nonetheless, in an ordered lattice, there are families of planes with different atomic occupation. This means that one atomic plane with one type of atom has the same direction as another atomic plane with a different type of atom. Families of planes are composed by planes with different scattering factors, depending of the type of atom forming each plane. Thus, the interference that occurs in ordered structures is not completely destructive, as is the case in disordered structures. The structure factor $F(\Delta k)$ will be not zero in case of order.

In summary, some intensity will appear on the so-called forbidden reflections when the structure is ordered.

Therefore, for the ordered structures it is necessary to redefine these extinction rules.

2.3.1. X-ray diffraction

X-ray diffraction due to the wavelength and nature of X-rays works best with policrystals and therefore is a bulk technique[9]. In fact, the first superlattices were described thanks to the analysis of X-ray diffractograms[28]. Before, it was supposed that order occurs at a Si-content of 25 at. %; subsequent X-ray investigations put the limit of ordering at 9 to 10 at. % Si [37].

In addition, diffuse scattering suggested the existence of short-range ordering in Fe-Si steels[10 and 55].

2.3.2. Neutron diffraction

Neutron diffraction theory is analogous to that of X-ray diffraction. But instead of photons the radiation is comprised of accelerated neutrons that are mostly sensitive to atomic cores instead of electrons. Also, neutron diffraction intensity does not depend of scattering angle like X-ray diffraction, and it can be used to investigate magnetic structure. Dynamics of phase transformations are studied by analysing the changes in superlattice diffraction peaks while increasing the temperature of the sample. This is an advantage over X-ray diffraction, because the measurement time is reduced by saving the annealing time necessary in X-ray diffraction.

Early studies of neutron diffraction, together with specific heat studies[47] provided with experimental transition temperatures within the BWG approximation. The calculation of these transition temperatures, T_x and T_y, gave shape to the paramagnetic region of the phase diagram[46], as studied in section 1.2 (Statistical treatment of order).

At this respect, the analysis of Daniel Ruiz *et al.*[56] revealed the disappearance of $D0_3$-related peaks at temperatures near 730 °C, while B2-related peaks persisted in a sample of 12.41 at. % Si (Fig. 5). The authors therefore concluded that the (dominant) structure is B2 at higher temperatures in high-silicon alloys. Notwithstanding, neutron diffraction experiments by[45] argued against the existence of B2 order in high-silicon samples; for 7.6 and 9.83 at. % Si

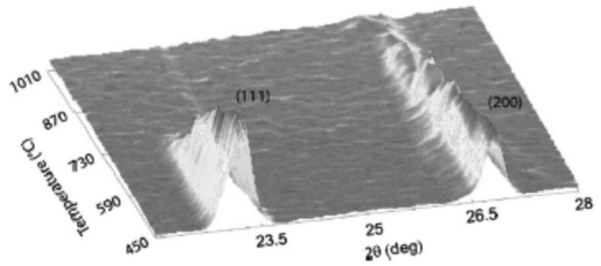

Figure 5. Neutron diffraction spectrum with an incident wavelength of 0.13 nm. Evolution of superlattice peaks with temperature (T) during the heating cycle of Fe-14 at. % Si (from[56]). Measurements were taken while heating the sample up to 1050 °C at a rate of 5 °C/min.

Figura 5. Espectro de difracción de neutrones, longitud de onda incidente 0,13 nm. Evolución de picos de super-red en función de la temperatura (T) durante un ciclo de calentamiento de Fe-14 at .% Si (de[56]). Las medidas fueron tomadas para un calentamiento de 5 °C/min hasta 1.050 °C.

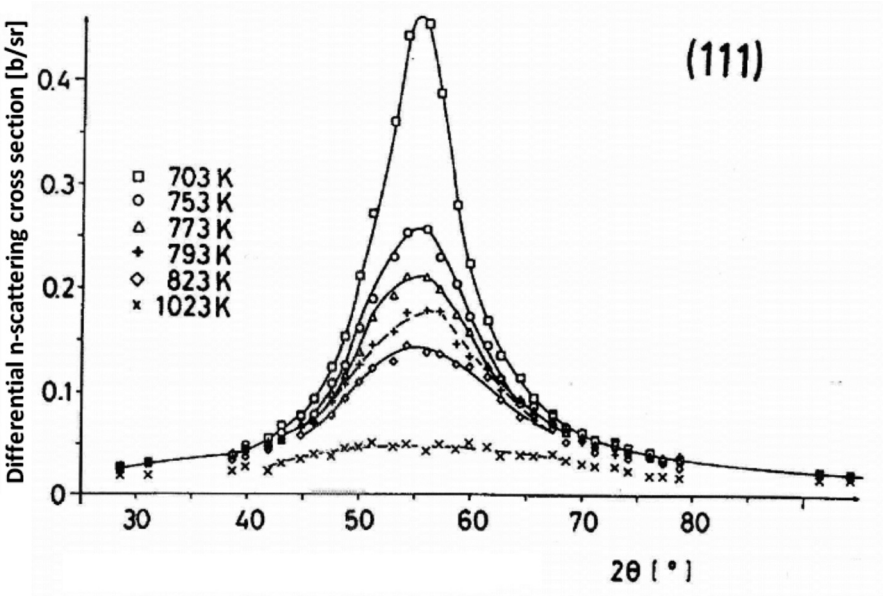

Figure 6. Neutron diffraction showing weak superlattice reflection corresponding to $D0_3$ ordering in a Fe-9.83 at. % Si during heating (from[45]). Importantly, this data casts doubts on the reliability of the established phase diagram for the Fe-Si system for this Si content (Fig. 2) where only B2 order is indicated.

Figura 6. Difracción de neutrones mostrando una débil reflexión de super-red, correspondiente al orden $D0_3$ en Fe-9,83 at %. Si durante calentamiento (de[45]). Notablemente, estos resultados siembran dudas en la fiabilidad del diagrama de fases establecido para el sistema Fe-Si para este contenido de Si (Fig. 2), donde sólo se indica orden B2.

they reported appearance of (111) reflections, present only in the $D0_3$ order and absent from the B2 order (Fig. 6)[45].

2.3.3. *Transmission Electron Microscopy (TEM)*

Transmission electron microscopy contributed in two major ways to the shaping of the phase diagram of the Fe-Si system. Firstly, through diffraction experiments, TEM helped to define the types of ordering found in the material and their limits. And secondly, through imaging, it led to the description of the B2 ordering and the double phase field (marked with a white arrow, Fig. 2).

In order structures the limits between the ordered and disordered zones are called domain boundaries. On the other hand, an ordered lattice may shift its periodicity in such a way that the sublattice corresponding to one kind of atom turns into a sublattice corresponding to another kind of atom. In this case, a surface forms where the phase shift takes place, although order is maintained. This surface is usually more energetic than the rest of the lattice, and receives the name of an anti-phase boundary (APB). In general, it is possible to detect these boundaries by dark field imaging (DF). The detection of APBs will be explained in the following sections regarding image analysis.

2.3.4. *Diffraction analysis*

The as-cast Fe-12.41 at. % Si was annealed in an oven at atmospheric pressure in air at 650 °C for 1 h, followed by water quench to room temperature. This ensures that the material will be in the double-phase region of the phase diagram. Surface oxidation was removed during standard sample preparation. The diffraction pattern indicates the presence of ordering before the annealing (Fig. 7) but, after annealing, it shows also of diffuse scattering between the Bragg sites (Fig. 8).

Short-range ordering produces such diffuse scattering in selected area diffraction (SAD)

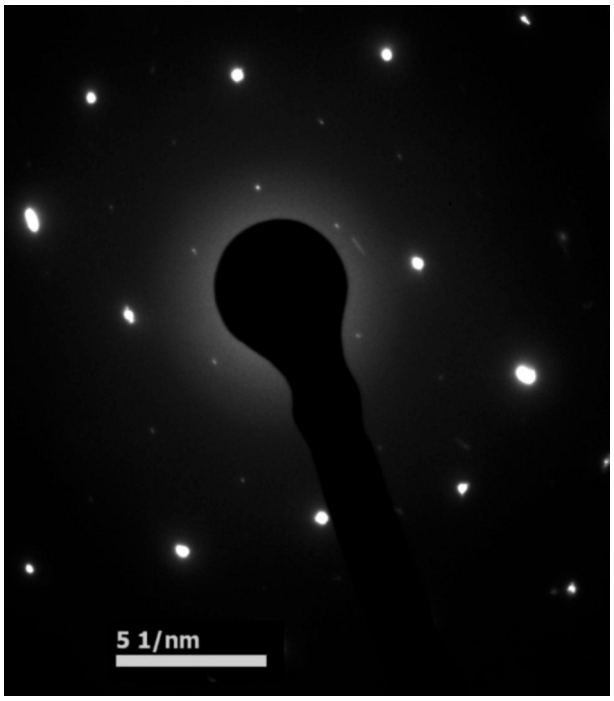

Figure 7. Diffraction pattern of as-cast Fe-12.41 at .% Si. Superlattice spots appear due to $D0_3$ order, zone axis [110].

Figura 7. Patrón de difracción de Fe-12,41 at. % Si de fundición. Reflexiones de super-redes aparecen debido al orden $D0_3$, eje de zona [110].

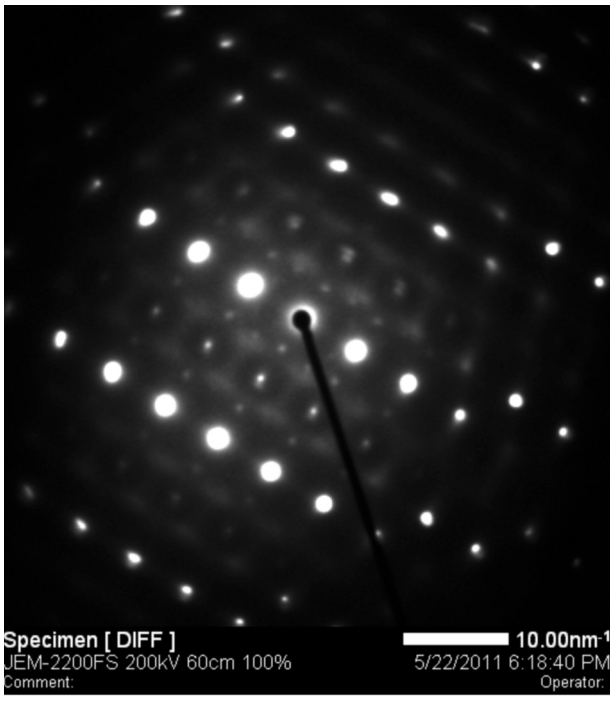

Figure 8. Fe-12.41 at. % Si after 1 h annealing at 650 °C and then quenching. Diffuse scattering may indicate presence of short range order in zone axis [211].

Figura 8. Fe-12,41 at. % Si después de 1 h de recocido a 650 °C y templado. La dispersión difusa podría indicar la presencia de orden a corto alcance en el eje de zona [211].

patterns[57]. The fact that superlattice reflections and diffuse scattering appear in the same zone may be interpreted as existence of small zones of ordering separated by disordered matrix and anti-phase boundaries. The diffuse scattering is not obvious in all the zone axes but the ordering is congruent with their orientation in figure 9.

Notice that upon annealing at 950 °C, the superlattice peaks do not disappear, as shown in the diffraction pattern of figure 10, upper right corner. For such Si-content (12.41 at. %) and quenching temperature (950 °C), the sample should not present order. A similar effect has been observed in other works[51]. Three factors may be responsible for this apparent contradiction:

– The quenching could not avoid ordering. Not probable because the small sample was quenched in water.

– The sample suffered segregation, creating a zone of at least 14 at. % in a region from where the TEM specimen was taken from. Superlattice peaks are very sharp, so the sample may be well into the order region. The required segregation would be too far from the nominal Si-content.

– The ordering starts at lower Si-contents than the ones predicted in the phase diagram, probably short-range order.

The appearance of clear superlattice peaks and surrounding satellites indicate that the most likely factor is the last one, although the second is possible too.

To summarise the foregoing, certain experimental data cannot be explained by the established phase diagram for the Fe-Si system (Fig. 2). They include neutron diffraction experiments showing (111) superlattice reflections for compositions and temperatures where only B2 order is expected[45]. Furthermore, certain ordering was unexpectedly found using TEM in literature, although the authors explained it by silicon segregation to local zones with higher ordering[51].

Short range order appears when quenching over transition temperatures[28]. The number of unlike-atom pairs is higher than for the randomised distribution of atoms. The experimental confirmation of diffuse scattering, typical for the short range order, is scarce. Diffuse scattering of figure 8 supports the hypothesis of this short range ordering.

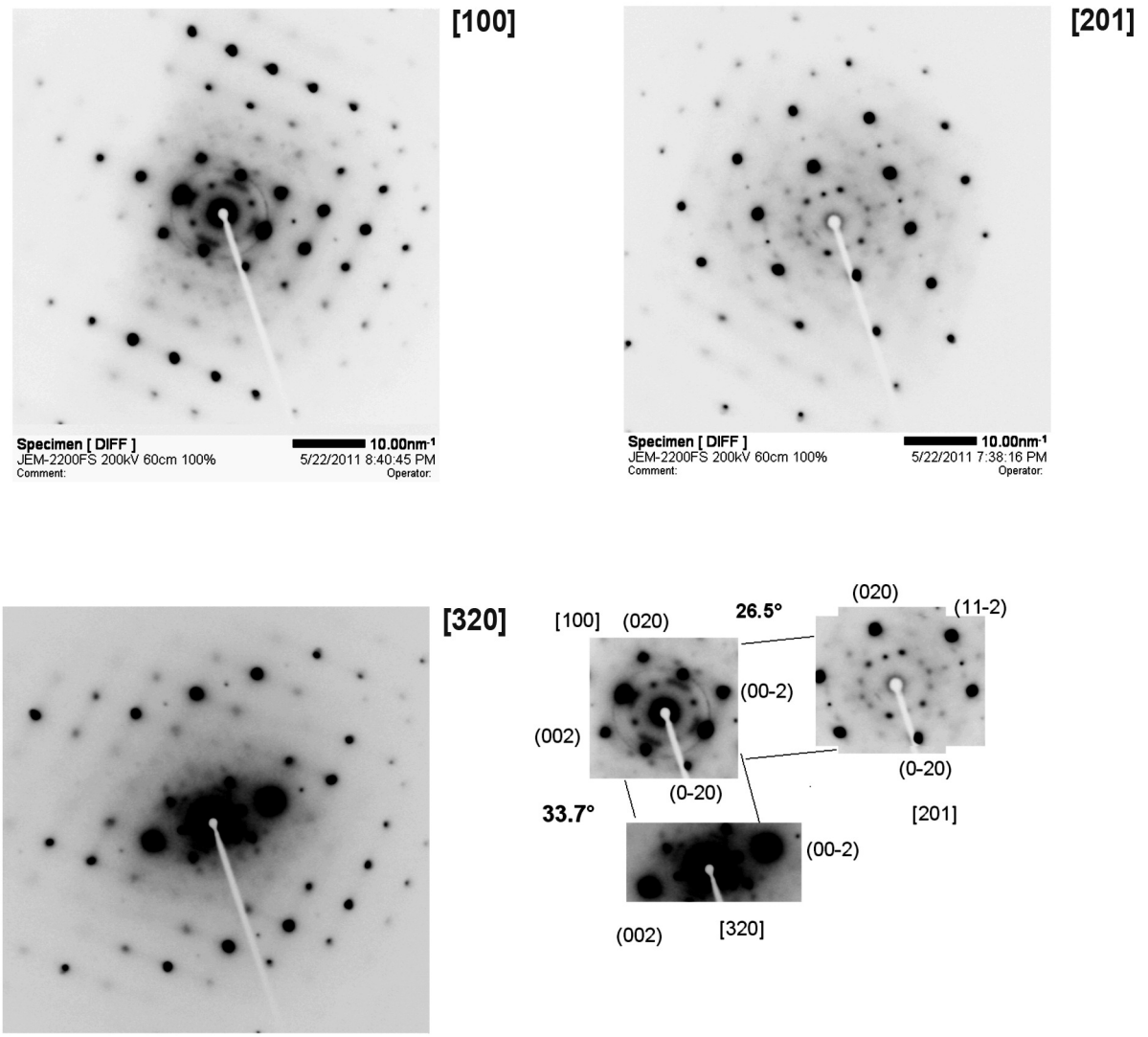

Figure 9. Zone axes orientation for Fe-12.41 at. % Si after 1 h annealing at 650 °C and quenching. The forbidden reflections and satellites appear in each zone axis.

Figura 9. Orientación de ejes de zona de Fe-12,41 at .% Si después de 1 h de recocido a 650 °C y templado. Las reflexiones prohibidas y satélites están presentes en cada eje de zona.

2.3.5. Image analysis

Anti-phase boundaries appear in the matrix when the periodicity of an ordered lattice suffers a shift, either due to annealing or deformation as explained below. The contrast of APB is normally low and invisible if the image is formed by all the beams. When contrast is more important than crystallographic features, the image should be formed only by the transmitted beam, which interacts with no atomic plane in the matrix. In the case of APBs, they are surfaces laid on atomic planes so they are detected by dark field (DF) imaging. Dark field imaging shows the contrast arising from one set of planes (the image is formed by one diffracted beam, the rest being blocked). If the imaged set of planes contains APBs, these features will be revealed in the DF micrograph.

APB image analysis is well established[58]. They can be classified according to the lattice direction of the phase shift. In an ordered lattice, there are two mechanisms of formation of APBs:

– if two ordered zones grow enough and meet each other, there is a possibility that they follow the same order but on different crystallographic "right" sites. The intersection zone presents a shift in the ordering.

– if one dislocation crosses an ordered structure, atoms jump to the contiguous sites, producing a shift in the lattice.

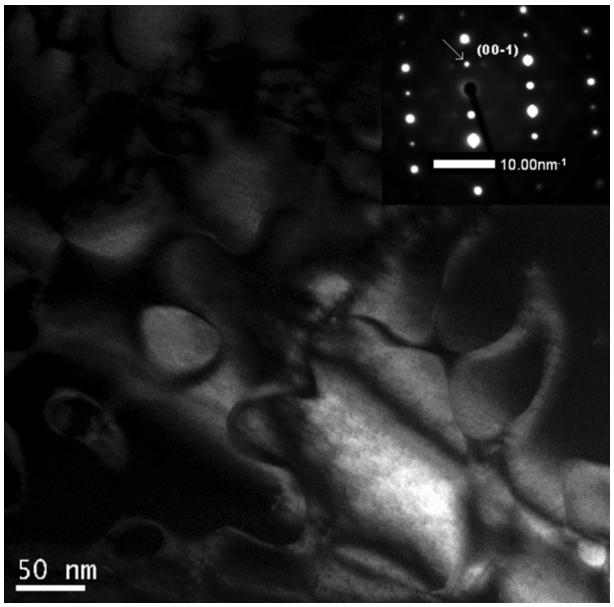

Figure 10. Fe-12.41 at. % Si after 950 °C annealing and quench. Dark field imaging on the selected spot (001), zone axis [210].

Figura 10. Fe-12,41 at .% Si después de recocido a 950 °C y templado. Imagen de campo oscuro con el punto seleccionado (001), eje de zona [210].

In any case, APBs are surfaces characterised by an order shift. For example, in figure 1, if the sites with preference for silicon jump to the nn positions, the direction of the shift is <111>, then the APB has <111> character. This is the only possible APB for the B2 ordering[59 and 60] and can be revealed by dark field imaging of B2 superlattice spots. They present non-crystallographic character, usually ribbon-shaped. An example of this APB can be found in figure 10.

Two types of APB can be described in a $D0_3$ lattice, following the <111> and the <100> direction, and this depends of whether silicon atoms jump to the nn or to the nnn[58 and 61].

The fact that crystallographic and non-crystallographic APBs appear in dark field is the main experimental confirmation of the theory of the double-phase region. While both kinds of APBs have been found in the double-phase region, only the non-crystallographic <111> APB is present in the α_2 region[32, 48 and 60].

Domain size strongly depends on Si-content and thermal treatment. Anti-phase boundaries disappear from the image when the size of the ordered domains reaches the size of the grain[60].

Some regions of the crystal, most likely situated at the interface of ordered zones, have different energy than others, so during electrochemical polishing they will be more attacked, and will be revealed in bright field imaging. To the best of our knowledge, this phenomenon was reported only by Antonin Gemperle before in a silicon iron alloy with similar content to the image presented in figure 11 [60]. These etched regions resemble the characteristics and topology of APBs: they are crystallographic lines (mosaic structure identified as <100> APBs) intermingled with larger, non-crystallographic lines (ribbon structure identified as <111> APBs). The existence of these APBs has been confirmed in various experiments and presents the main support for the existence of a double-phase region. Nonetheless, it is advisable to bear in mind that both types of APBs are possible in $D0_3$ ordered domains.

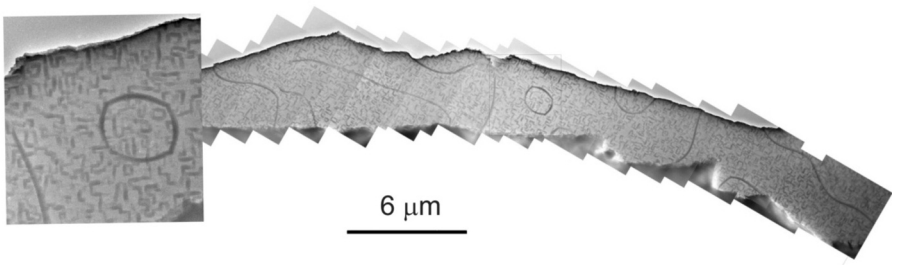

Figure 11. Fe-12.14 at. % Si in the as-cast state, bright field image showing mosaic crystallographic structure and ribbons following non-crystalline directions in an extensive area.

Figura 11. Fe-12,14 at .% Si de fundición, imagen de campo claro mostrando estructura cristalográfica en mosaico y lazos en direcciones no cristalinas en un área extensa.

3. MECHANICAL AND MAGNETIC PROPERTIES

Embrittlement of silicon steel was its first reported characteristic[1]. The slip lines observed in deformed silicon steel have a wavy character and disappear for Si-contents over 7.65 at. % due to lowering of the stacking fault energy[62], thus making dislocation glide more difficult. This is one of the reasons for rise of brittleness.

In addition, dislocation movement forms APBs. The energy rises, and order should be re-established with another dislocation. When it is energetically favourable, APBs may link the first dislocation with another dislocation or form a group of four dislocations, depending on the type of ordering. Partial dislocations would move together forming a superdislocation. In general, if the APB energy is high, the partial dislocations will be close to each other, making slip and recombination easy. If it is too low, the dislocations would dissociate into simple dislocations, leaving APBs behind. Superdislocations shall be stable for intermediate APB energy, when cross-slip would be difficult and dislocations will show a tendency to pile up[63]. For instance, in Fe-Al alloys no superdislocations were observed[58] but they are present in Fe-Si alloys (although in Fe-Al alloys ordering rises after 20 at. % of Al-content, almost double than silicon, indicating than silicon tends to form order much more than aluminium). The general mechanism responsible for the formation of dislocation pairs is the contribution of ordering in the form of linking APBs rather than stacking fault energy[64].

Short range order, as already explained, is the tendency for solute atoms to arrange so they have more dissimilar neighbours than they would have if the distribution was random. Movement of dislocations in short range ordered regions reduces local order. This disordering will increase the energy of the alloy, and more deformation energy is hence needed[65].

3.1. Embrittlement and ordering

It has been reported that when the sample presents $D0_3$ ordering, the ductility decreases more than if the sample was quenched from the B2-zone of the diagram[66]. As the temperature increases, the order is reduced, so it is expected that brittleness is reduced too. It is considered that ordering is unavoidable after a Si-content 25 at. % (stoichiometric Fe_3Si) independently of the temperature at which the alloy is quenched.

Deformation experiments linked the amount of silicon to the promotion of twinning, believed to be caused by higher order in casted samples[67].

Being an analysis technique sensitive to local neighbouring atoms, the evaluation of Mössbauer spectra for the estimation of changes in long-range order is not straightforward. It is possible to make a correlation between long range order and the local ordering. The results would hint the lower threshold of long range order. Of course, a bulk diffraction technique is more suitable for the measurement of long range order, for example X-ray diffraction in transmission mode. In any case, long-range order parameters (section 1.2) were estimated from Mössbauer spectra as a function of deformation, as shown for several silicon contents[67] in figure 12. The fitting of $Fe_{15}Si$ for long range order does not significantly change with respect to the as-cast state. The $D0_3$ long range order, on the other hand, is reduced for Si-contents 8 and 9.5 at. %, but increases for Si-contents above 12.14 at. %. Hence, deformation reduces long range $D0_3$ order for high silicon contents to lesser extent than for low Si-contents, probably due to the destruction of ordering through shearing.

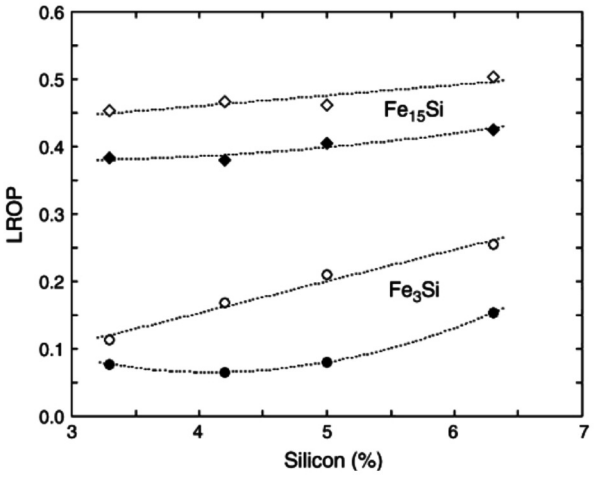

Figure 12. Long range order parameter as a function of Si content considering $Fe_{15}Si$ and Fe_3Si configurations, obtained from Mössbauer spectra for the undeformed (hollow symbols) and deformed (full symbols) after cold deformation for samples with different Si-contents[67].

Figura 12. Orden a largo alcance en función del contenido de Si considerando las configuraciones de $Fe_{15}Si$ y Fe_3Si, obtenido del espectro Mossbauer en muestras sin deformar (símbolos vacíos) y después de deformación en frío (símbolos rellenos) para muestras con distintos contenidos de Si [67].

It is expected that dislocation movement does not affect heavily the short-range ordering but may negatively affect the long-range order through generation of anti-phase boundaries (APBs). Indeed, for $D0_3$ order four dislocations with the same Burgers vector are required for the reconstruction of the superlattice and avoiding of APB formation[64].

In summary, long range order is more likely to be diminished by deformation than short-range order, specially at Si-contents higher than 10 at. % (5.3 mass. %) which is normally considered the limit value for long-range order formation[61].

3.2. Positron annihilation and EBSD. Deformation, recovery and recrystallisation

Positron Annihilation Lifetime Spectroscopy (PALS) is based on the measurement of the lifetime of positrons annihilating due to interaction with electrons in a material. A general description of the technique can be found in[68]. Relevant information like density of defects and their sizes are obtained from the number of positrons annihilated at a given lifetime. The lifetime of the positron gives the type of the defect size (and hence, type of defect), and the number of positrons annihilated with such lifetime gives information about the defect density. In a defect-free material, all positrons would annihilate with a characteristic lifetime of 108 μs. Higher lifetimes would indicate the presence of defects, normally vacancies or clusters of vacancies.

Another way to obtain information about defects from positron annihilation is by Doppler broadening (shape parameter analysis). The shape of the spectrum of core-electron annihilations will differ from the spectrum corresponding to annihilations with valence electrons. This shape parameter S will increase with the amount of vacancies, reflecting the fact that more positrons annihilate with valence (unbound) electrons.

Both measurements detect vacancies and clusters of vacancies. These vacancies can be related to dislocation density and lattice strain[69].

PALS and Doppler broadening gave the same results when analysing deformed samples after several annealing stages on a deformed sample containing 13.88 at. % Si [70 and 71]. Defect concentration decreases with temperature up to 400 °C (static recovery). Between 400 and 650 °C, there is a plateau where vacancies are not destroyed, and it is believed the dislocation movement is restrained due to ordering. For temperatures higher than 650 °C, near the onset for disordering, the vacancy number decreases again until it is considered defect-free at 900 °C [70]. In addition, there is an increase of the S parameter for temperatures between 400 and 600 °C [71] (Fig. 13). It is supposed that a new type of defect forms, probably vacancy clusters. These clusters would form during the approaching of dislocations, before dislocation annihilation between 650 and 700 °C.

These results from positron annihilation were combined with Electron Backscatter Diffraction (EBSD). EBSD is a diffraction technique that scans the sample surface, measuring local orientation. It is possible to analyse average misorientation, texture and local changes in orientation produced by twinning, shear bands, grain boundaries, etc.

EBSD preliminary data shows no strong changes in texture or kernel average misorientation below 700 °C. Temperatures over 700 °C produce recrystallisation[70]. High deformation will store high energy, so annealing temperatures near 900 °C will produce recrystallisation and grain growth rather than only recovery.

Other studies[72] were performed on steel with lower Si-content (~12 at. % Si) based on mechanical spectroscopy (internal friction) combined with neutron diffraction and DSC. It was found that

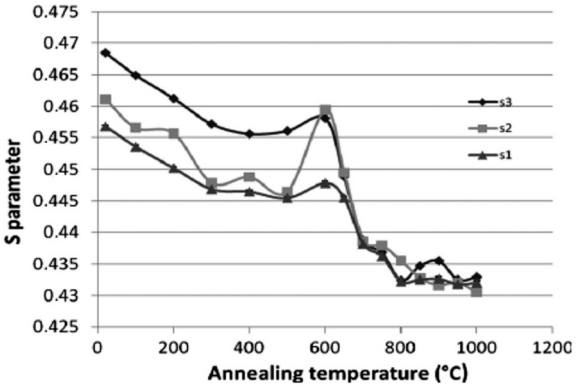

Figure 13. Evolution of the positron lifetime shape line with annealing temperature for three different deformations[71]. The increase of the S-parameter between 500 and 650 °C indicate the formation of a new type of defect (vacancy cluster) probably due to proximity and grouping of dislocations.

Figura 13. Evolución de la forma de la línea de vida media de positrones en función de la temperatura de recocido para tres deformaciones distintas[71]. El aumento del parámetro S entre 500 y 650°C indica la formación de un nuevo tipo de defecto (grupos de vacantes) probablemente debido a la proximidad y agrupación de dislocaciones.

movement of grain boundaries is impeded due to dislocation piling, but recovery process starts near 530 °C. As expected, the amount of silicon influences dislocation mobility through two main contributions, the increase in Peierls Nabarro force and the ordering, which raises stacking fault energy[73]. The influence of ordering in stacking fault energy has been studied in other ordered alloys[74]. Decreasing overall ordering would increase dislocation mobility.

Recrystallisation is an important part of the manufacture of grain oriented silicon steels[13]. There are applications in which the magnetic flux does not change within the steel, so instead of optimising the magnetic properties via increasing of Si-content, the material is made highly anisotropic, with the preferred orientation {110} <001>, to obtain optimal magnetic properties and minimum core loss in one direction. This special texture is obtained via control of precipitates and recrystallisation and/or texture control during primary recrystallisation. These steels present similar characteristics of order-disorder as the non-oriented counterpart[75].

3.3. Twinning and order

At low Si-content, the main deformation mechanism is dislocation movement, for room temperatures. It seems that, when the amount of silicon increases in solid solution, dislocation movement is impeded. Twinning becomes prominent in FeSi alloys at a Si-content near 4 mass % [76 and 77], or approximately 8 at. %. Ordering makes twinning difficult especially for ordered alloys ($s > 0.5$). For instance, the Fe_3Al system did not show twins after impact deformation at -196 °C if the degree of order was high, $s > 0.5$, but when $s < 0.5$ (disorder) profuse twinning was detected[28]. Although twinning and slip-assisted twinning is a typical mechanism of deformation at Si-contents of about 3-4 mass % (between ~6 and ~9 at. % Si)[78], the further addition of silicon increases the critical temperature for twinning[61]. Consistently, most results indicate that for high silicon samples (over 9-10 at. % Si) twinning is not detected using EBSD for any deformation rate (Fig. 14).

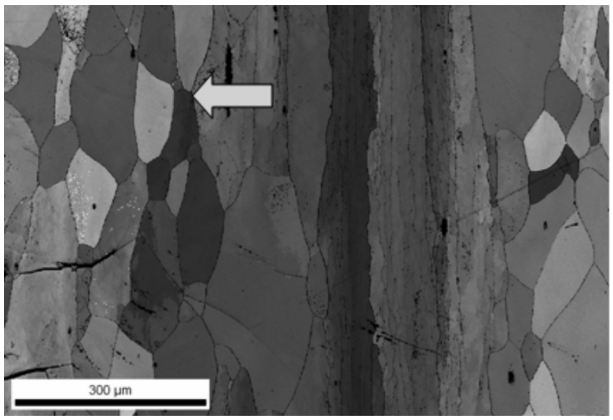

Figure 14. Fe-13.88 at. % Si, as deformed, 2 % deformation. The only twin found is marked with an arrow.

Figura 14. Fe-13,88 at .% Si deformado, 2 % de deformación. El único signo de maclado está marcado con una flecha.

3.4. Room temperature ageing

Steel working includes several steps as heating and reducing thickness of a sheet, using a rolling mill. After hot rolling the steel sheet may be at temperatures of 800 °C and cold rolling is normally required to improve its thickness and properties. The speed of cooling after the hot rolling is particularly important: if the steel cools down slowly, order degree increases as ordered state is stable in equilibrium, making cold rolling more difficult. Hence, the steel is cooled down very fast to keep the degree of order at a minimum, which facilitates subsequent cold rolling.

In addition, not only the speed of cooling is crucial, but also the time lapse between the hot and cold rolling influences brittleness of the Fe-Si steel, as discovered during experiments with thermo-mechanical routes[53]. Hot rolled steel sheet left for few hours can develop cracks during cold rolling[67] independently of the cooling rate after hot rolling[79] (Fig. 15 and Fig. 16).

Two possible mechanisms could explain this: room temperature strain ageing and room temperature short-range ordering.

Strain ageing is a common occurrence in steels. Upon deformation, the carbon atoms move towards dislocations, forming Cortrell-Bilby atmospheres. If the deformation stops and then continues the stress-strain curve continues too, but if there is an idle time between the first deformation and the second, the carbon atoms have time to relax to the interstitial positions, increasing the strength of the alloy. This effect occurs for an idle time of several days at room temperature, but takes few hours if the deformation cycles are performed at 150 °C (hence the name "bake hardening").

The presence of silicon increases the activity of carbon[80]. Therefore, the time at which strain ageing takes place at room temperature may be drastically reduced due to higher activity of carbon, induced by the high Si-content. This effect may be related to interpass ageing, an effect of carbide precipitation

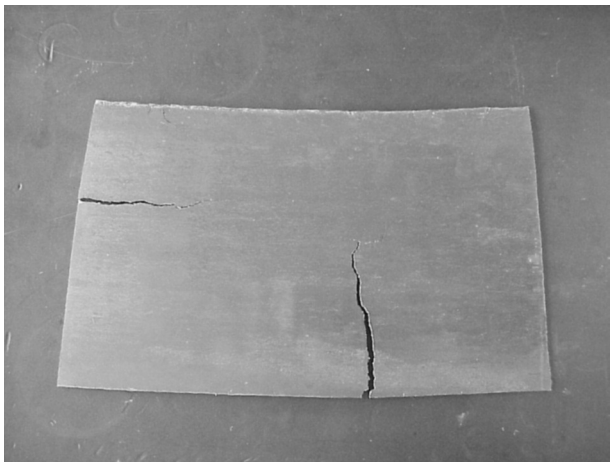

Figure 15. Cracks in high silicon steel after 3 h idle time between hot rolling and cold rolling[79].

Figura 15. Grietas en acero de alto silicio después de 3 h de espera entre laminado en caliente y en frío[79].

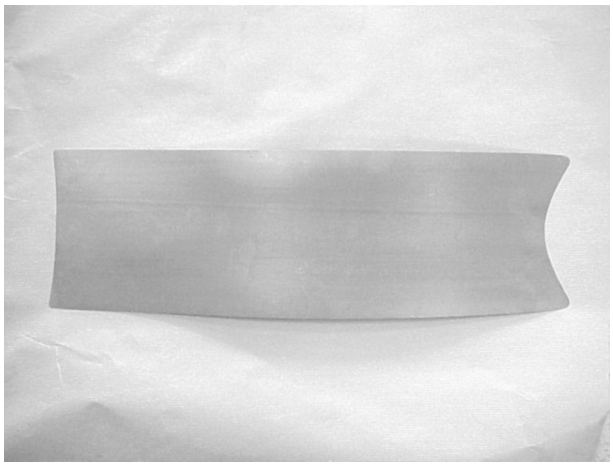

Figure 16. High silicon steel sheet after cold rolling immediately after hot rolling[79].

Figura 16. Plancha de acero de alto silicio laminado en frío inmediatamente después de laminación en caliente[79].

observed during rolling and quenching of grain oriented silicon steel[13].

In any case, this phenomenon has been observed in silicon steel samples with relatively low carbon concentration (less than 100 ppm in most cases). Hence, there is another proposed mechanism that explains the idle time-caused embrittlement through the formation of short range order by local order of silicon atoms. The phenomenon is known as room temperature short-range ordering, named after the temperature at which it was observed. The silicon interdiffusion depends of the relative compositions and the self-diffusion coefficients, according to Darken's equation as studied in[81]. Other measurements of diffusion, based on electron microprobe, show the influence of ordering in diffusion: according to Heikinheinmo[82], the interdiffusion increases with Si-content in the disordered region, decreases slightly in the double-phase region of the phase diagram and increases again in the ordered (α_1) region. The diffusion cannot be studied at low temperatures due to lack of a suitable silicon radioisotope[81], but the interdiffusion is estimated by extrapolation to have a value of 2.5×10^{-23} [m^2/s] at room temperature, from the values obtained by Rabkin *et al.*[83]. This corresponds to roughly 1 jump/h on average.

Locally, the silicon atoms may reduce the Gibbs energy by forming a structure with a configuration similar to equilibrium, which is an ordered configuration. This effectively reduces the distance between silicon atoms that are postulated to form pair-like structures (Zener pairs).

Both possibilities are analysed using internal friction (IF). Internal friction is a mechanical spectroscopic technique that gives information about the concentration of impurities in solution. Its basic principle is the measurement of the phase shift between a periodic deformation and the response of the material. The internal friction 1/Q is proportional to the concentration of impurities and their type, which is associated with a characteristic frequency[84 and 85]. For instance, at room temperature, carbon in solution is associated with a peak near 0.15 Hz while nitrogen in solution is associated with a peak near 1 Hz. All the measurements were taken at room temperature, varying the frequency.

The effect of time on the amount of carbon in solid solution (which forms the Cotrell-Bilby atmospheres) can be seen in figure 17, where the Snoek peak of carbon decreases steadily after the Ultra Low Carbon (ULC) steel was quenched from high temperature[86].

Different contributions to the spectrum come from interstitial atoms (Snoek-type peaks) and from the interaction between substitutional atom pairs (Zener-type peaks), see[87]. In the case of figure 18, there is a small quantity of nitrogen in solution which appears at its characteristic frequency, near 1 Hz. Asymmetrical peaks indicate normally superposition of two peaks[88]. Hence, two more peaks can be described at lower frequencies[86 and 89], which correspond to the interstitial-substitutional coupling C-Si and Si-Si Zener relaxation. These Si-Si couples may be in positions that would form short-range ordering for silicon contents under 9.5 at. %, in accordance with

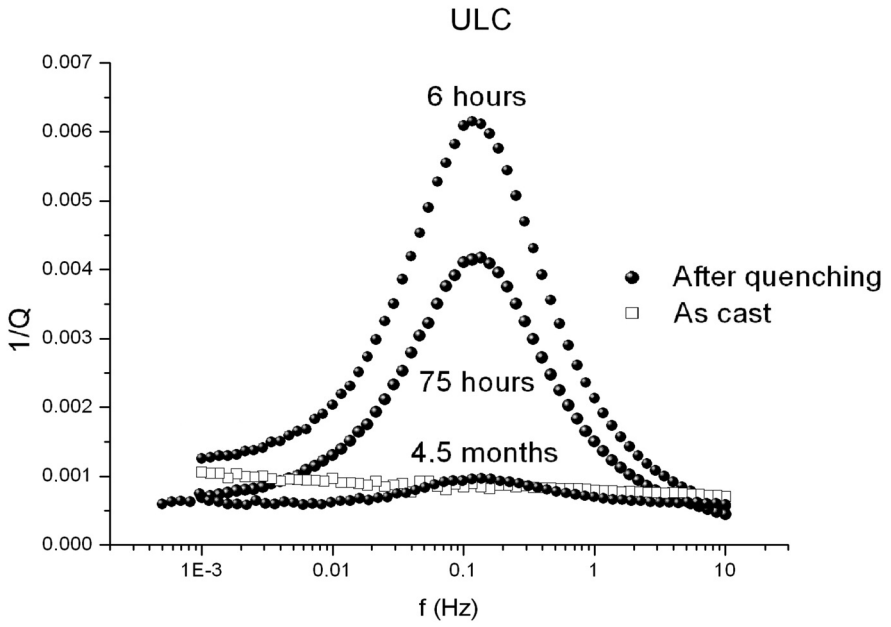

Figure 17. ULC steel showing carbon peak. Measurements taken at different times (6 hours, 75 hours and 4.5 months) after quenching from 900 °C [86]. All measurements taken at room temperature.

Figura 17. Acero ultra bajo en carbono mostrando un pico de carbono. Las medidas fueron tomadas en distintos momentos (6 horas, 75 horas y 4,5 meses) después de templado desde 900 °C [86]. Medidas realizadas a temperatura ambiente.

the diffraction experiments (Fig. 8). Whether these peaks form at room temperature directly after quenching cannot be discussed due to the weakness of the signal (which leads to high error).

3.5. Influence of ordering on electric and magnetic properties

One of the main problems in soft magnetic materials with industrial applications is the losses. Nowadays, typical losses of commercial steels are in the range of 1.5 or 2 W/Kg (at 1.5 T, 50 Hz) and 2.5 (1.5 T, 60 Hz) for a hysteresis energy of 250 to 320 J/m^3 [90]. These low losses have been reached thanks to research and optimization of thermomechanical routes. For example, losses can be improved from 4.4 W/kg to 3.7 W/kg by decreasing the reheating temperature from 1260 °C to 1150 °C and the coiling temperature from 760 °C to 670 °C [91] in a regular commercial silicon steel. The total energy losses can be divided into hysteresis loss, classical loss and anomalous loss[5 and 6]. Many parameters affect losses in different ways. For example, the skin depth increases with resistance (hence, with Si-content), but it is inversely dependant on frequency[92], and losses would increase if the grain size is too small, even at high frequencies, but the grain size is influenced by silicon content[93 and 94]. Even the way of cutting the piece seems to have an important influence in hysteresis[95].

One of the positive influences of silicon in the alloy, with respect the magnetic properties, is the increase in resistivity while at the same time reducing magnetostriction and energy loss[10 and 96]. This effect may be directly related to ordering: a sample with low ordering presents higher resistivity although short range ordering has the opposite influence[97]. Saturation magnetostriction (the cause of the characteristic "humming" in electric devices) is practically zero at 12.2 at .% Si, making vibration almost disappear. This is expected, as magnetostriction is one of the mechanisms of energy dissipation, and this energy will be low if the hysteresis cycle is narrow (which is one of the main characteristics of soft magnetic materials).

Nonetheless, the influence of ordering in magnetic properties is not clearly established. It seems that ordering has lesser influence than grain size, so the effect of ordering is normally noticeable in steels with

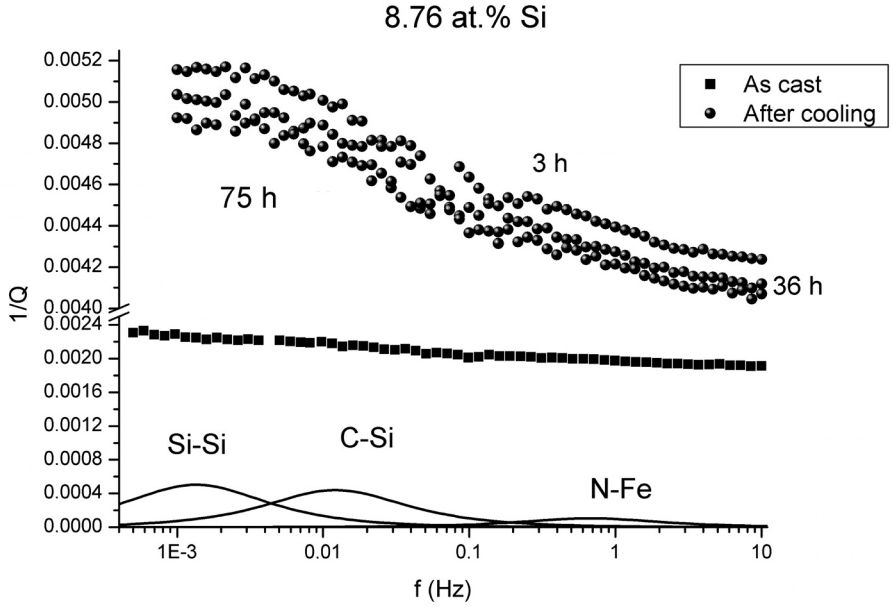

Figure 18. Electrical steel with a Si-content of 8.7 at. % showing peaks corresponding to carbon-silicon and silicon-silicon pairs[86].

Figura 18. Acero eléctrico con contenido en silicio de 8,7 at. %, mostrando las señales correspondientes a las parejas carbono-silicio y silicio-silicio[86].

small grain size[66]. Ordering has an incremental effect on conductivity as disordered (quenched) alloys have higher electrical resistance than ordered alloys. For example, powdered Fe-15 mass. % Si (Fe_3Si) samples with high degree of order showed a resistivity of 50 μΩ/cm while for a quenched state the resistivity is 150 μΩ/cm [97]. It is well established that $D0_3$ ordering causes deterioration of magnetic properties in magnetic permeability experiments[98] and as such, high maximum permeability is obtained after rapid quench from 500 °C for Si-contents near 12 at. %, although a strong D03 ordering decreases magnetostriction[41]. Magnetic moment of iron depends on the position in the lattice: for iron atoms surrounded by iron, the value is close to 2.4 μ_B while for atoms surrounded by iron and silicon atoms ($D0_3$ configuration), the value drops to approximately 1.3 μ_B [99] according to neutron diffraction measurements. These experimental values are in agreement with *ab initio* simulations[100] Apparently, $D0_3$ ordering is more stable due to a total reduction of the energy as compared to other type of orderings as B2.

4. CONCLUSIONS

— Silicon steels are soft magnetic materials composed by iron and silicon in a relation between 3.8 at. % and approximately 15 at. % Si (the system is considered an intermetallic compound for contents near and over 25 at. % Si). Their structure is based in the body centered cubic lattice. Their magnetic properties have been studied since the beginning of 20th century. Despite their industrial importance (low magnetostriction, low hysteresis losses, high permeability, etc), silicon steels are far from providing the optimal soft-magnetic properties due to the brittleness they show when the Si-content exceeds 5.8 - 6.3 at. % (3 - 3.5 mass %).

— Ordering is described in silicon steels as dependent of composition and temperature. There is a stable second-order ordering transformation for contents over approximately 10 at. % for temperatures near 500 °C.

— The traditional phase diagram shows B2-type ordering between the disordered region and the $D0_3$ region. This ordering proved to be responsible of the high brittleness of Fe-Si alloys due to resistance of the lattice to dislocation movement.

— Nonetheless, ordering may be stable at concentrations of silicon lower than those appearing in the phase diagram. Due to the low Si-content, it is normally regarded as short-range order. This is due to the tendency of silicon atoms to be surrounded by iron atoms at least up to the second neighbour.

— The B2 denomination gives the impression of the formation of a stable order phase, instead of being a step previous to the long-range $D0_3$ order. The use of the alternative notation (α_2 for B2 and α_1 for $D0_3$) is encouraged. In addition, said B2-type ordering region may be thinner, if it exists at all.
— But ordering reactions are not limited to equilibrium conditions. Experimental diffraction patterns show that for contents at which ordering is not expected diffuse scattering and superlattice reflections appear. The cause of these reflections may be the local formation of silicon couples as a previous configuration for $D0_3$ ordering. This formation of ordered structures would explain the embrittlement of Fe-Si steel at Si-contents lower than the predicted by the phase diagram.

REFERENCES

[1] T.D. Yensen, *University of Illinois Bulletin XIII* (1915).
[2] J.A. Ewing, *Magnetic Induction in Iron and Other Metals*, The Electrician Printing and Publishing Co. Limited, London, 1900.
[3] G.A.V. Sowter, *J. Audio Eng. Soc.* 35 (1987) 760-777.
[4] T.D. Yensen, *University of Illinois Bulletin* (1914) 70.
[5] R.M. Bozorth, *Ferromagnetism*, MacMillan, London, 1951.
[6] B.D. Cullity, *Introduction to Magnetic Materials*, Addison-Wesley Publishing Company, Reading, Mass., 1972.
[7] C.E. Birchenall, *Thermodynamics in Physical Metallurgy*, American Society of Metals, Cleveland, 1950.
[8] T. Muto and Y. Takagi, *Order-disorder Phenomena in Metals*, F. Seitz and D. Turnbull (Eds.), Academic Press, 1955, pp. 193-282.
[9] B.D. Cullity, *Elements of X-Ray Diffraction*, Addison-Wesley Publishing Company, Inc., Notre Dame, Indiana, 1956.
[10] S. Guruswamy, G. Garside, C. Ren, B. Saha and M. Ramanathan, *Prog. Cryst. Growth Ch. Mater.* 57 (2011) 43-64.
[11] E.S. Greiner, J.S. Marsh and B. Stoughton, *The Alloys of Iron and Silicon*, First Edit, McGraw - Hill, New York and London, 1933.
[12] C.P. Yap, *J. Phys. Chem.* 37 (1932) 951-967.
[13] M. Matsuo, *ISIJ Int.* 29 (1989) 809-827.
[14] J.E. May and D. Turnbull, *Transactions of the Metallurgical Society of AIME* 212 (1958) 769-781.
[15] J.E. Thompson, *Reviews of Physics in Technology* (1970) 27-46.
[16] A.F. Filho, C. Bolfarini, Y. Xu and C.S. Kiminami, *Scripta Mater.* 42 (1999) 213-217.
[17] G. Tian and X. Bi, *Surf. Coat. Tech.* 204 (2010) 1295-1298.
[18] K. Verbeken, I. Infante-Danzo, J. Barros-Lorenzo, J. Schneider and Y. Houbaert, *Rev. Metal.* 46 (2011) 458-468.
[19] T. Ros-Yanez, M.D. Wulf and Y. Houbaert, *J. Magn. Magn. Mater.* 272-276, Supplement (2004) E521 - E522.
[20] A.F. Filho, C. Bolfarini, Y. Xu and C.S. Kiminami, *Scripta Mater.* 42 (2000) 213-217.
[21] S. Crottier-Combe, S. Audisio, J. Degauque, J.L. Porteseil, E. Ferrara, M. Pasquale and F. Fiorillo, *J. Magn. Magn. Mater.* 160 (1996) 151-153.
[22] M. Rebhan, M. Rohwerder and M. Stratmann, *Appl. Surf. Sci.* 140 (1999) 99-105.
[23] M. Jitsukawa and Y. Hosoya, *NKK Technical Review* 88 (2003) 46-57.
[24] M. Abe, K. Okada and S. Fukuda, *Method of Chemical Vapor Deposition in a Continuous Treatment Line*, U.S. Patent 5352490, EE.UU., 1994.
[25] M. Enokizono, N. Teshima and K. Narita, *IEEE T. Magn. Mag.* 18 (1982) 1007-1013.
[26] K.I. Arai and Y. Yamashiro, *J. Appl. Phys.* 64 (1988) 5373-5375.
[27] V. Gavriljuk, *Acta Mater.* 48 (2000) 3879-3893.
[28] N.S. Stoloff and R.G. Davies, *Prog. Mater. Sci.* 13 (1968) 1-84.
[29] G. Inden, and W. Pitsch, *Z. Metallkd.* 62 (1971) 627-632.
[30] G. Inden, *Acta Metallurgica* 22 (1974) 945-951.
[31] K. Momma and F. Izumi, *J. Appl. Crystallogr.* 41 (2008) 653-658.
[32] P.R. Swann, L. Grånäs and B. Lehtinen, *Metal Science* 9 (1975) 90-96.
[33] O. Kubaschewski, *Iron-binary Phase Diagrams*, Springer-Verlag, Berlin, 1982.
[34] E. Heikinheimo, A.A. Kodentsov and F.J.J. van Loo, *Acta Metallurgica* 38 (1998) 1229- 1235.
[35] G. Papadimitriou and J.M. Genin, *Phys. Status Solidi A* 9 (1972) K19-K23.
[36] T. Ros, D. Ruiz, Y. Houbaert and R.E. Vandenberghe, *J. Magn. Magn. Mater.* 242-245 (2002) 208-211.
[37] M.C.M. Farquhar, M.A. Lipson and A.R. Weil, J. *Iron Steel Institute* 152 (1946) 457-471.
[38] Y.F. Liang, J.P. Lin, F. Ye, Y.J. Li, Y.L. Wang and G.L. Chen, *J. Alloy Compd.* 504, (2010) S475-S479.

[39] K. Raviprasad, K. Aoki and K. Chattopadhyay, *Mater. Sci. Eng. A* 172 (1993) 125-135.
[40] J.H. Yu, J.S. Shin, J.S. Bae, Z.H. Lee, T.D. Kee and H.M. Lee, *Journal of Korean Institute of Metals and Materials* 39 (2001) 394-398.
[41] K. Narita and M. Enokizono, *IEEE T. Magn.* 15 (1979) 911-915.
[42] I.N. Shabanova, V.I. Kormilets, L.D. Zagrebin and N.S. Terebova, *J. Struct. Chem.* 39 (1998) 1098-1102.
[43] E.G. Moroni, W. Wolf, J. Hafner and R. Podloucky, *Phys. Rev. B* 59 (1999) 860-871.
[44] A.I. Al-Sharif, M. Abu-Jafar and A. Qteish, *Condens. Matter Phys.* 13 (2001) 2807.
[45] K. Hilfrich, W. Kölker, W. Petry, O. Schärpf and E. Nembach, *Scripta Metallurgica et Materialia* 24 (1990) 39-44.
[46] G. Inden and W. Pitsch, *Z. Metallkd.* 63 (1972) 253-258.
[47] H.H. Ettwig and W. Pepperhoff, *Z. Metallkd.* (1972) 453-456.
[48] G. Schlatte and W. Pitsch, *Z. Metallkd.* 67 (1976) 462-466.
[49] J. Lacaze and B. Sundman, *Metallurgical Transactions A* 22A (1991) 2211.
[50] L.D. Landau and E.M. Lifshitz, *Física Estadística* Vol. 5, Editorial Reverté, 1969.
[51] J.S. Shin, J.S. Bae, H.J. Kim, H.M. Lee, T.D. Lee, E.J. Lavernia and Z.H. Lee, *Mater. Sci. Eng. A* 407 (2005) 282-290.
[52] W.J. Yuan, R. Li, Q. Shen and L.M. Zhang, *Mater. Charact.* 58 (2007) 376 - 379.
[53] T. Ros-Yanez, D. Ruiz, J. Barros, Y. Houbaert and R. Colas, *Mater. Sci. Eng. A* 447 (2007) 27-34
[54] B. Fultz and J.M. Howe, *Transmission Electron Microscopy and Diffractometry of Materials,* 3rd Edition, Springer, 2008.
[55] N.V. Ershov, V.A. Lukshina, B.K. Sokolov, Y.P. Chernenkov and V.I. Fedorov, *J. Magn. Magn. Mater.* 300 (2006) 469-472.
[56] D. Ruiz, T. Ros-Yañez, G.J. Cuello, R. Vandenberghe and Y. Houbaert, *Physica B-Condensed Matter.* 385 (2006) 578-580.
[57] M.D. Graef, *Introduction to Conventional Transmission Electron Microscopy*, Cambridge University Press, 2003.
[58] M.J. Marcinkowski and N. Brown, *Acta Metallurgica* 9 (1961) 764-786.
[59] A. Gemperle and J. Kočik, *Phys. Solid. State* 19 (1967) 333.
[60] A. Gemperle, *Transactions of the Metallurgical Society of AIME* 242 (1968) 2287.
[61] G. Lakso and M.J. Marcinkowski, *Metallurgical Transactions* 5 (1974) 839-845.
[62] T. Saburi and S. Nenno, *Philos. Mag.* 15 (1967) 813-824.
[63] F.J. Humphreys and M. Hatherly, *Recrystallization and Related Annealing Phenomena*, Elsevier Ltd, Oxford, 2004.
[64] L. Grånäs and B. Aronsson, *Transactions of the Metallurgical Society of AIME* 239 (1967) 1273-1274.
[65] G.E. Dieter, *Mechanical Metallurgy*, McGraw - Hill, 1988.
[66] F. Faudot, J.F. Rialland and J. Bigot, *Phys. Scripta* 39 (1989) 263-267.
[67] T. Ros-Yáñez, D. Ruiz and J. Barros, *Mater. Sci. Eng. A*, 447 (2007) 27-34.
[68] J.M. Campillo and F. Plazaola, *Defect Diffus. Forum* 141 (2003) 213–215.
[69] D. Porter and K.E. Easterling, *Phase Transformations in Metals and Alloys*, CRC Press, 1992.
[70] F. González, K.M. Mostafa, R. Petrov, P.R. Calvillo, E.D. Grave, D. Segers and Y. Houbaert, *Int. J. Mater. Res.* 103 (2012) 1440-1443.
[71] K.M. Mostafa, F. González Camara, R. Petrov, P. Rodriguez Calvillo, J. De Baerdemaeker, E. De Grave, D. Segers and Y. Houbaert, *J. Appl. Phys.* 151 (2011) 960-963.
[72] O.A. Lambri, J.I. Pérez-Landazábal, J.A. Cano and V. Recarte, *Mater. Sci. Eng. A* 370 (2004) 459-463.
[73] B. Viala, J. Degauque, M. Fagot, M. Baricco, E. Ferrara and F. Fiorillo, *Mater. Sci. Eng. A* 212 (1996) 62.
[74] O.A. Lambri, J.I. Pérez-Landazábal, V. Recarte, G.J. Cuello and I.S. Golovin, *J. Alloys Compd.* 537 (2012) 117-122.
[75] K. Hilfrich, O. Schärpf and E. Nembach, *J. Appl. Phys.* 74 (4) (1993) 2354-2358.
[76] F. Sorbello, P.E.J. Flewitt, G. Smith and A.G. Crocker, *Acta Mater.* 57 (2009) 2646-2656.
[77] P.R. Calvillo, R. Petrov, Y. Houbaert and L. Kestens, *Mater. Sci. Forum* 550 (2007) 539.
[78] J. Prahl, A. Machová, M. Landa, P. Hausild, M. Karlík, A. Spielmannová, M. Clavel and P. Haghi-Ashtiani, *Mater. Sci. Eng. A* 462 (2007) 178-182.
[79] Y. Houbaert and J. Schneider, *3rd International Conference WMM'08*, J. Schneider, Y. Houbaert and K. Verbeken (Eds.), Ghent, Belgium 2008.
[80] L.S. Darken, *Trans. AIME* 180 (1948) 430-438.
[81] H.V.M. Mirani and P. Maaskant, *Phys. Status Solidi* A14, 521 (1972) 521-525
[82] E. Heikinheimo, A.A. Kodentsov and F.J.J. van Loo, *Scripta Mater.* 38, 8 (1998) 1229-1235.
[83] E. Rabkin and W. Gust, *Thermodymanics of Alloy Formation*, Y. A. Chang, and F. Sommer, (Ed.), Minerals, Metals & Materials Soc, Warrendale, EE.UU., 1997, pp. 199-219.

[84] A. Nowick and B. Berry, *Anelastic relaxation in crystalline solids*, Academic Press, 1972.
[85] R. Schaller, G. Fantozzi and G. Gremaud (Eds.), *Mechanical Spectroscopy 2001*, Trans. Tech. Publications, Switzerland, 2001.
[86] F. González, D. Ruiz and Y. Houbaert, *11th International Conference of Imperfections Interaction and Anelastic Phenomena in Solids*, Trans. Tech. Publications, Tula, Rusia, 2007, p. 8.
[87] M.S. Blanter, I.S. Golovin, H. Neuhäuser and H.-R. Sinning, *Internal Friction in Metallic Materials,* Springer Verlag, 2007.
[88] I.S. Golovin, H. Neuhäuser, H.-R. Sinning and C. Siemers, *Intermetallics* 18 (2010) 913-921.
[89] D. Ruiz, J.L. Rivera-Tovar, D. Segers, R.E. Vandenberghe and Y. Houbaert, *Mater. Sci. Eng. A* 442 (2006) 462-465.
[90] F. Landgraf, M. Emura and M. Decampos, *J. Magn. Magn. Mater.* 320 (2008) e531-e534.
[91] G. Lyudkovsky and P.D. Southwick, *Metallurgical Transactions A* 17 A (1986) 1267-1275.
[92] S. Constantinides, *4th International Conference WMM'10*, J. Schneider and R. Kawalla (Eds.), Ghent, Belgium 2010.
[93] G. Bertotti, *IEEE T. Magn.* 24 (1988) 621-630.
[94] S. Paolinelli, M.A. Cunha, R. Takanohashi and A.M. Simões, *4th International Conference WMM'10*, J. Schneider and R. Kawalla (Eds.), Ghent, Belgium 2010.
[95] M. Emura, F.J. Landgraf, W. Ross and J. Barreta, *J. Magn. Magn. Mater.* 254-255 (2003) 358-360.
[96] R. Brajpuriya, P. Sharma, S. Jani, S. Kaimal, T. Shripathi, N. Lakshmi and K. Venugopalan, *Appl. Surf. Sci.* 257 (2010) 10-16.
[97] F.W. Glaser and W. Ivanick, *Journal of Metals* (1956) 1290-1295.
[98] W. Ciurzy ska, J. Zbroszczyk, J. Olszewski, J. Frackowiak and K. Narita, *J. Magn. Magn. Mater.* 133 (1994) 351-353.
[99] N.I. Kulikov, D. Fristot, J. Hugel and A.V. Postnikov, *Phys. Rev. B* 66 (2002) 1-8.
[100] S. Dennler and J. Hafner, *Phys. Rev. B* 73 (2006) 1-14.